Journal of Polymers and the Environment
https://doi.org/10.1007/s10924-023-03123-2

ORIGINAL PAPER

Durable and Low-Cost Chitosan Decorated Fe/MOF-5 Bimetallic MOF Composite Film for High Performance of the Congo Red Adsorption

Eman M. Abd El-Monaem[1] · Ahmed M. Omer[2] · Abdelazeem S. Eltaweil[1]

Accepted: 30 October 2023

Abstract

The auspicious merits of polysaccharides make them eminent choices in numerous fields, particularly water remediation. Nonetheless, polysaccharides like chitosan (CTS) suffer from low adsorbability. Meanwhile, the recent revolution in material science has produced substances with supreme adsorbability, such as metal-organic frameworks (MOFs). Consequently, the Fe/MOF-5@CTS composite film was synthesized by doping a low amount (5 wt%) of Fe/MOF-5 into the CTS film. The crystallinity, morphology, composition, and surface charge of the Fe/MOF-5@CTS composite film were identified using multiple characterization analyses. Furthermore, the adsorption property of Fe/MOF-5@CTS was examined for the removal of Congo red (CR). Surprisingly, the Q_{max} of CR onto Fe/MOF-5@CTS reached 219.78 mg/g. Additionally, the composite film only lost 18.54% of its capacity after ten cycles. The selectivity test demonstrated the higher selectivity of the positively charged-rich composite film towards anionic dyes, especially CR, compared to the cationic dyes. Based on the practical experiments and analysis tools, the adsorption mechanism of CR onto Fe/MOF-5@CTS is presumed to occur via electrostatic, host-guest, π-π interaction, and coordination bonds.

Keywords MOF-5 · MOF-53(Fe) · Chitosan · Composite film · Congo red · Selectivity

Introduction

The twenty-first century is witnessing significant growth in heavy industries, which is prospering the economy of some countries. Aside from this bloom, the discharged wastewater from these industries tends to be a major catastrophe for the world. Dyes play a quintessential role in industries such as plastic, printing, paper, pharmaceutical, and textiles [1]. Nonetheless, the majority of synthetic dyes are stable and noxious which complicates their removal.

Congo red is one of the most harmful synthetic dyes due to its complicated structure, which enhances its stability in water and thus inhibits light permeability [2, 3]. Therefore, the presence of CR in water poses a serious threat to marine life. The CR dye has deleterious effects on human health, including eye irritation, blood clotting, gene mutation, cancer, diarrhea, and more [4].

Accordingly, various remediation techniques have progressed to remove CR effluents from water, including coagulation [5, 6], adsorption [7], ozonation [8, 9], catalysis [10], and membrane [11, 12]. Notably, the facile operation, low cost, uncomplicated design, and adsorbents' reusability make adsorption the most preferred remediation method [13].

Obviously, MOFs have gained researchers' consideration for their unrivaled features comprising outstanding chemical and thermal stability, as well as high porosity and surface area [14, 15]. Interestingly, MOFs are distinguished by their ease of functionalization without experiencing any collapse or partial collapse of their frameworks [16]. Hence, MOFs have exhibited advanced performance in diverse potential applications like catalysis, sensors, gas storage, drug delivery, water purification, and so on [17]. In particular,

✉ Ahmed M. Omer
amomar@srtacity.sci.eg

✉ Abdelazeem S. Eltaweil
abdelazeemeltaweil@alexu.edu.eg

[1] Chemistry Department, Faculty of Science, Alexandria University, Alexandria 21321, Egypt

[2] Polymer Materials Research Department, Advanced Technology and New Materials Research Institute (ATNMRI), City of Scientific Research and Technological Applications (SRTA-City), P. O. Box: 21934, New Borg El-Arab City, Alexandria, Egypt

Published online: 14 November 2023

the MOFs' stability in aqueous media and their super-high aptitude towards versatile contaminants render them a perfect choice as premium adsorbents. Excessive developments have proceeded on MOFs to enhance their adsorption performances; for instance, fabricating binary MOF [18], bimetallic MOF [19], and MOFs composites [20].

Among the remarkable MOFs, MOF-5, also known as IRMOF-1, stands out with its well-ordered structure, porosity, flexible functionalization, and thermal stability [21]. MOF-5 is constructed from zinc (as the core metal) and 1,4-benzene dicarboxylic acid (as the linker). The applications of MOF-5 have expanded to various fields, including water purification, gas storage, catalysis, gas separation, and drug delivery [22]. Furthermore, MIL-53(Fe) has shown promising results in these applications due to its flexibility, chemical stability, and remarkable adsorption capabilities [23]. MIL-53(Fe) is built using iron as the core metal and 1,4-benzene dicarboxylic acid as the linker. Unfortunately, there are still obstacles in using MOFs as adsorbents, which limits their applications on a large scale, including high cost and poor recyclability.

Chitosan (CTS) is a notable branch in the polysaccharides realm, possessing remarkable features, such as nontoxicity, natural availability, good hydrophilicity, cost-effectiveness, and prime adsorption efficacy [24]. In addition to the ease of preparing CTS from chitin, which is derived smoothly from abundant and cost-effective resources, such as insects, shrimp, fungi, crabs, algae, and so on [25]. Notably, CTS has a unique structure that facilitates its functionalization through the presence of surface-reactive functional groups (viz., OH and NH_2), as well as its texture that enables it to take on various forms (such as membranes, spheres, fibers, films, etc.). However, it suffers from low adsorption performance and weak durability when used without proper modifications.

Doping the chitosan film with MOF material enhances its adsorption and durability by increasing the available adsorption sites and introducing metal centers, leading to improved performance as an adsorbent.

Our work intended to exploit the advantages of MOFs to improve the adsorption capacity of CTS. Subsequently, Fe-doped MOF-5 was incorporated into the CTS film, forming an efficacious adsorbent with a good reusability feature for removing CR from aqueous solutions. In detail, Fe-doped MOF-5 was fabricated with Fe ion ratios of 0, 25, 50, 75, and 100% (pure MIL-53(Fe)). Importantly, the optimum ratio of Fe-doped MOF-5 incorporated into the CTS film was examined at a bimetallic MOF ratio of 1–10 wt%. Furthermore, the Fe/MOF-5@CTS composite film was characterized morphologically, thermally, and texturally. A comprehensive batch study of CR adsorption onto the Fe/MOF-5@CTS composite film was conducted. Additionally, the impact of ionic strength on the CR adsorption was assessed, and the selectivity and reusability tests were performed.

Experimental Work

Materials

Text S1 compiles the used materials in the preparation of Fe/MOF-5@CTS composite film.

Preparation of Fe/MOF-5

Dissolving of 1.664 g of $Zn(NO_3)_2{\cdot}6H_2O$ in 60 mL DMF for 15 min, then 0.352 g of H_2BDC was dipped in the Zn^{2+} solution. After 20 min, a certain proportion of $FeCl_3{\cdot}6H_2O$ (0, 25, 50, 75, and 100 wt%) was added to the Zn^{2+}/H_2BDC solution, and the mixture was stirred for an additional 20 min. Thereafter, the resultant suspension was transferred to an autoclave and kept under heating for 24 h at 120 °C. Ultimately, the obtained MOF was separated, washed by DMF and C_2H_5OH, and dried at 80 °C overnight.

Preparation of Fe/MOF-5@CTS Composite Film

Fe/MOF-5@CTS composite film was prepared by dissolving CTS (2% wt/V) in 20 mL Dist. H_2O (2% V/V AcOH). Then, a calculated mass of Fe/MOF-5 (1–10 wt%) was added bit-by-bit to the CTS solution and kept for 2 h under continuous stirring and sonication for 30 min. Next, Fe/MOF-5@CTS composite film was poured into a petri dish and stored until completely dry of the composite film. To remove Fe/MOF-5@CTS from the petri dish, an aqueous NaOH solution (5% wt/V) was poured onto the sticky composite film. After 1 h, Fe/MOF-5@CTS composite film could be smoothly removed from the petri dish and washed thoroughly by Dist. H_2O, and dried at room temperature. Noteworthy, the CTS film was fabricated by the same former procedure without adding MOF. The schematic representation for the fabrication of Fe/MOF-5@CTS composite film is shown in Fig. 1.

Characterization Instruments

Fe/MOF-5@CTS composite film, CTS film, and pure MIL-53(Fe) and MOF-5 were analyzed by Powder X-Ray Diffraction (PXRD-MAC Science M03XHF, XRD) to scrutinize crystallite phase of the samples. In addition, the morphologies of Fe/MOF-5@CTS composite film and their components were studied by Scanning Electron Microscopy (S4800-Hitachi, SEM), which was further utilized to explore the elemental composition of Fe/MOF-5@CTS composite film *via* the attached energy dispersive

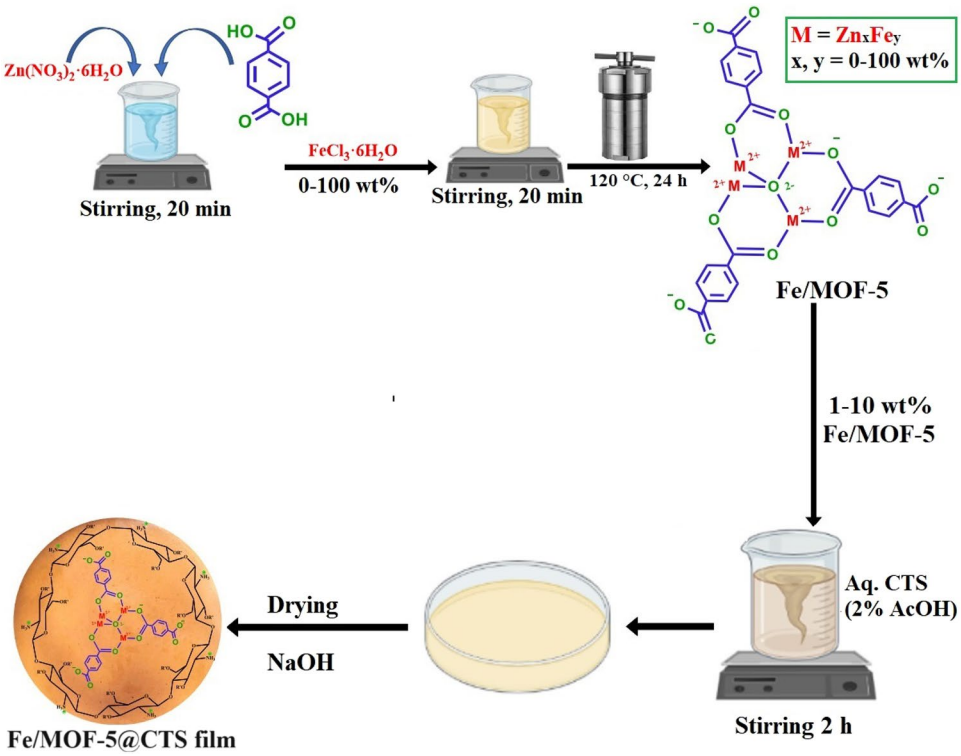

Fig. 1 Schematic representation demonstrating the synthetic approach for Fe/MOF-5@CTS composite film

x-ray part. Fourier Transform Infrared Spectrometer was used to define the functional groups of the samples. The surfaces charges were determined by Zeta Potential (Malvern, ZP), and X-Ray Photoelectron Spectroscopy assured the elemental composition of the samples (Thermo-Fisher Sci., XPS). The surface area and pore size of the samples was determined by Brunauer–Emmett–Teller method (Tristar II 3020, BET). Besides, the mechanical properties and thickness of films were investigated using universal testing machine (AG-1 S, Shimadzu, Japan) and a digital micrometer screw gauge (Ajanta, India), respectively.

Water Uptake Study

The water uptake behaviour of the pristine CTS and Fe/MOF-5@CTS films were inspected by soaking 0.1 g of tested film sample in distilled water (pH 7.2) at room temperature. At time intervals (0.5–3 h), the swollen sample was gently separated and blotted between two filter papers to remove the adhered surface water drops and finally followed with weighing in an electronic balance. The water uptake (WU; %) was calculated according to the following equation:

$$\mathrm{WU}\ (\%) = \frac{W_t - W_0}{W_0} \times 100 \tag{1}$$

where, W_0 is the initial weight of tested sample and W_t is the weight after time t.

The CR Removal Experiments

The removal process of CR by Fe/MOF-5@CTS composite film proceeded as follows; (i) Assess the pH influence on the removal efficacy of CR at a pH range between 3 and 11. (ii) Test the composite film's dosage impact on removal% at a range from 0.01 to 0.04 g. (iii) Identify the thermal performance of the CR/composite film system by changing the process temperature of the CR adsorption from 25 to 55 °C. (iv) Evaluate the isotherm of the CR adsorption onto Fe/MOF-5@CTS at a concentration range of 50–300 ppm. At the end of each experiment, a sample was withdrawn and measured via a spectrophotometer at 500 nm, and scrutinize the adsorption performance of Fe/MOF-5@CTS towards CR by applying the following equations:

$$\mathrm{Removal\%, R\%} = \frac{C_0 - C_t}{C_0} \times 100 \tag{2}$$

$$\mathrm{Adsorption\ capacity,\ } Q_t = \frac{(C_0 - C_t) \times V}{m} \tag{3}$$

The initial CR concentration is defined as C_o, while the final concentration symbolizes C_t. The weight of the used

composite film and the CR volume is represented by m and V, subsequently.

Ionic Strength

The influence of ionic strength on the adsorption capacity of CR adsorption onto Fe/MOF-5@CTS was assessed by introducing different concentrations of NaCl (ranging from 0 to 1.0 mol/L) into a solution of CR (20 mL, 100 ppm) and stirring for 5 min. Subsequently, the Fe/MOF-5@CTS composite film was immersed in the CR/NaCl solution. After 2 h samples were withdrawn to measure the remaining CR using a spectrophotometer.

Selectivity Test

The capacity of Fe/MOF-5@CTS composite film towards other anionic dyes like methyl orange (MO) and methyl red (MR) and also cationic dyes like crystal violet (CV) and methylene blue (MB) was assessed to prove the composite film's selectivity. The selectivity test proceeded by adding 0.02 g of Fe/MOF-5@CTS to 20 mL of the specific dye (100 mg/L). After 2 h, the concentrations of the un-adsorbed dyes were identified using UV–vis spectroscopy.

Cycling Test

The cycling test of Fe/MOF-5@CTS composite film was performed by soaking the CR-loaded composite film in methanol/1 M NaCl for 2 h. Next, the composite film was stored in the air to dry and reused in the next cycle.

Results and Discussion

Characterization of Fe25/MOF-5@CTS

PXRD

Figure 2 A clarifies the crystallite phases of the prepared samples. The PXRD of CTS film indicates its good crystallinity, as evidenced by the prominent peaks with high intensity at 2θ = 10° and 20°, corresponding to (240), and (273) planes [26, 27]. The PXRD profile of MOF-5 exhibits characteristic peaks at 2θ = 6.1°, 9.2°, 14.1°, 15.7°, 17.6°, 26.6°, 28.6°, 30.5°, 32.5°, 35.7°, and 38.9°, corresponding to the (200), (220), (400), (420), (333), (711), (731), (751), (911), (860), and (1022) planes, respectively [28, 29]. Moreover, characteristic peaks of MIL-53(Fe) were observed at 2θ = 9.3°, 12.5°, 17.8°, 25.1°, and 26.5°, corresponding to the (200), (110), (111), (220), and (221) planes, respectively [30]. The PXRD profile of Fe25/MOF-5 exhibits the main characteristic peaks of MOF-5, with a slight shift toward lower 2θ angles, along with the disappearance of some distinctive peaks of MOF-5. This observation confirms the successful doping of Fe ions into MOF-5, in agreement with Abo El-Yazeed et al. [31]. The PXRD profile of Fe25/MOF-5@CTS shows the characteristic peaks of CTS, without the appearance of the corresponding peaks of Fe25/MOF-5. This can be attributed to the low loading

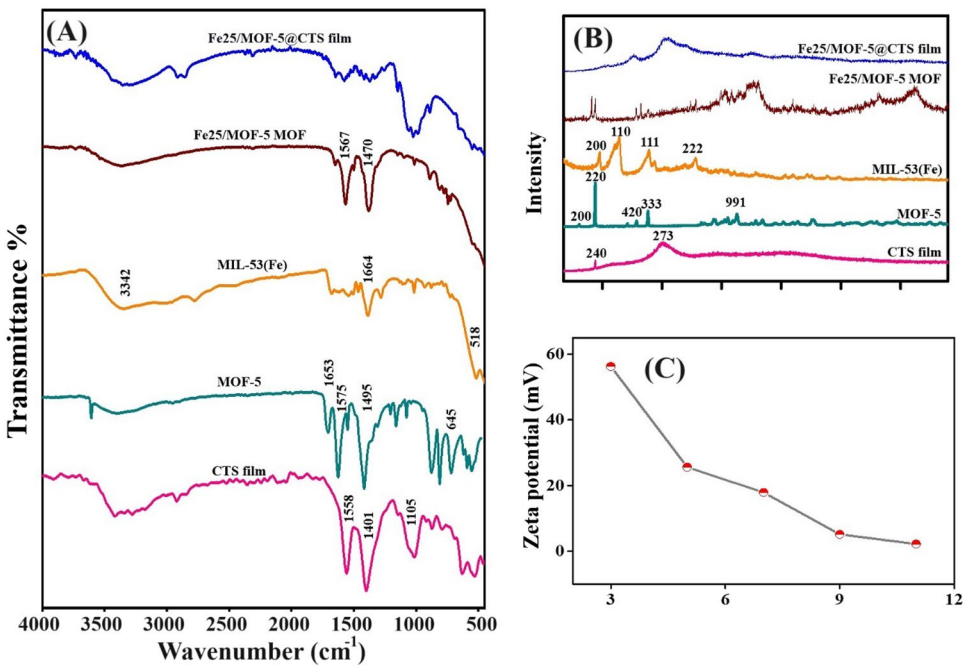

Fig. 2 **A** PXRD, and **B** FTIR of pure CTS film, MOF-5, MIL-53(Fe), Fe25/MOF-5 bimetallic MOF, and Fe25/MOF-5@CTS composite film, and **C** ZP of Fe25/MOF-5@CTS composite film

proportion of the bimetallic MOF in the CTS matrix and the good homogeneity and dispersion of Fe25/MOF-5 into CTS.

FTIR

Figure 2B illustrates the functional groups of the synthesized samples. The FTIR spectrum of CTS shows absorbance peaks at 1015, 1401, 1558, 2920, and 3417 cm^{-1}, which correspond to C–O–C, C–OH, N–H, C–H, and O–H bonds, respectively [32]. The FTIR spectrum of MOF-5 displays absorbance peaks at 645, 3597, and 1758 cm^{-1}, which are attributed to Zn4O, OH, and C–O bonds, respectively [29]. The peaks at 1495, 1572, and 1653 cm^{-1} are assigned to asymmetric C=O bonds, while the symmetric C=O bond appears at 1359 cm^{-1} [33]. The FTIR spectrum of MOF-53(Fe) reveals distinctive absorbance peaks at 518, 778, 1676, and 3342 cm^{-1}, which are attributed to Fe–O, C–H, C = O, and OH bonds. Additionally, peaks related to asymmetric and symmetric C–O bonds are observed at 1464 and 1505 cm^{-1} [34]. The FTIR spectrum of MOF-5 exhibits characteristic peaks with lower intensity and a peak shift toward higher wavenumbers, suggesting the successful doping of Fe ions into MOF-5. Furthermore, the appearance of peaks at 1470 and 1567 cm^{-1} reflects the formation of coordination bonds between the carboxylic groups of H2BDC and the central metal ions (Zn and Fe) [35]. The spectrum of Fe25/MOF-5@CTS shows absorbance peaks of Fe25/MOF-5 and CTS with lower intensity, indicating the homogeneity of the composite film.

ZP Measurements

The net carried charges on the surface of Fe25/MOF-5@CTS were evaluated by ZP measurements (Fig. 2C). Obviously, Fe25/MOF-5@CTS is highly charged with positive charges where the ZP attained 56.3 mV at pH 3. The ZP results revealed the suitability of Fe25/MOF-5@CTS to adsorb the anionic pollutants via the electrostatic forces.

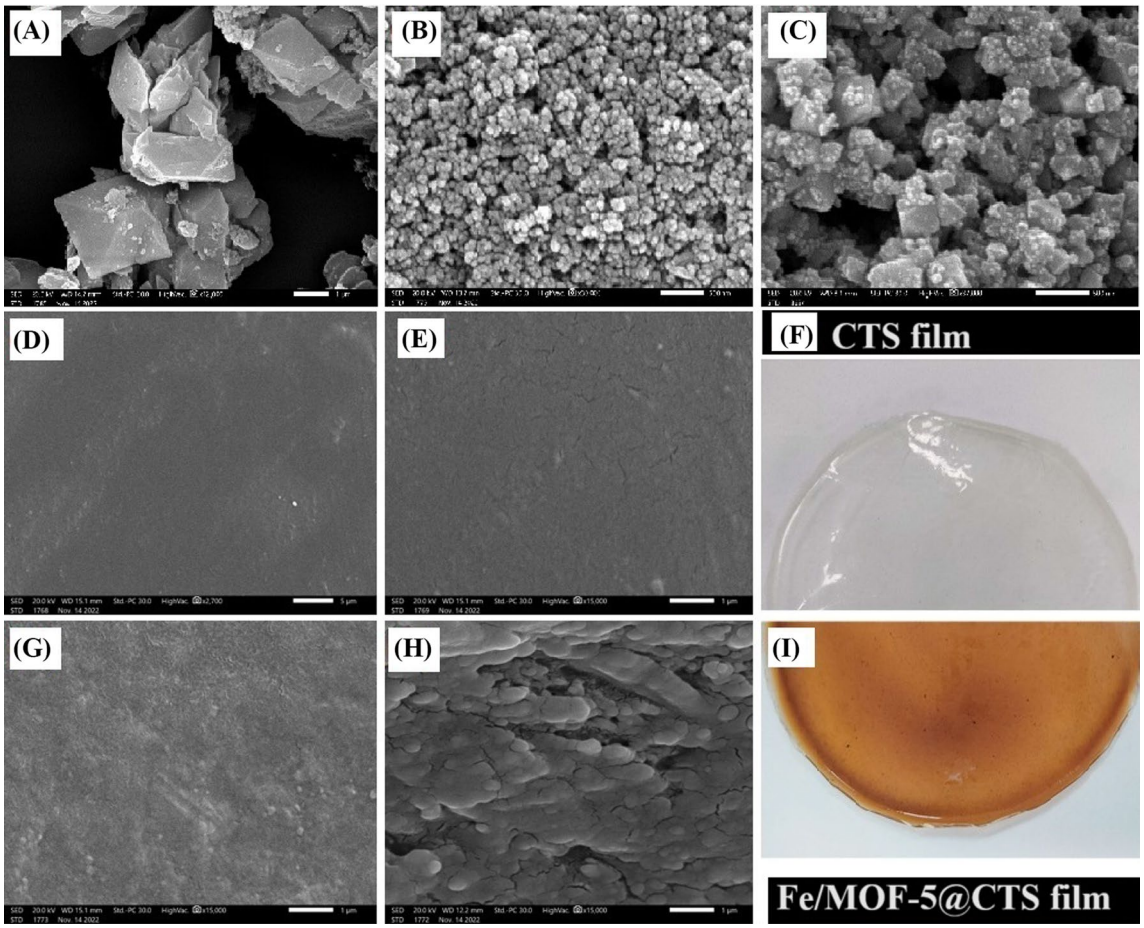

Fig. 3 SEM of **A** MOF-5, **B** MIL-53(Fe), **C** Fe25/MOF-5, **D** Air side, **E** Cross-sectional, and **F** Digital photo of CTS film, **G** Air side, **H** Cross-sectional, and **I** Digital photo of Fe25/MOF-5@CTS composite film

SEM

The morphologies of the fabricated samples were figured out via SEM (Fig. 3). As elucidated in Fig. 3A, the particles of MOF-5 have bipyramid-like morphology. The MIL-53(Fe) particles have a quasi-spherical morphology (Fig. 3B). The SEM image of Fe25/MOF-5 (Fig. 3C) showed poly morphologies of bipyramid and spherical, indicating the formation of the Fe25/MOF-5 bimetallic MOF. The SEM image of the air side of the pristine CTS film (Fig. 3D) revealed a flat and nonporous surface [36, 37]. The SEM of the cross-sectional pure CTS film (Fig. 3E) showed a smooth layer with some cracks. The SEM image of the air side of the Fe25/MOF-5@CTS composite film (Fig. 3G) elucidated a more rigid surface compared to the pristine CTS film, implying the positive role of Fe25/MOF-5 bimetallic MOF in boosting the mechanical strength of CTS film [38, 39]. Obviously, the cross-sectional Fe25/MOF-5@CTS composite film (Fig. 3H) showed distributed particles between the polymeric layers of CTS, inferring the incorporation of Fe25/MOF-5 into the CTS film. Figure 3F, I) points out digital photos of CTS and Fe25/MOF-5@CTS composite film. A slight change in film thickness was observed after the composite formation since the average thickness of the developed composite film recorded about 0.0894 mm compared to 0.081 mm for pure dried CTS.

BET Measurements

Figure 4 A elucidated the nitrogen adsorption/desorption isotherms of CTS, MOF-53(Fe), MOF-5, Fe25/MOF-5, and Fe25/MOF-5@CTS. The isotherms depict that all the fabricated samples are mesoporous substances since the isotherms represent type (IV) with H4. The S_{BET} of CTS, MOF-53(Fe), MOF-5, Fe25/MOF-5, and Fe25/MOF-5@CTS were 41.34, 157.81, 189.26, 645.49, and 516.54 m2/g, respectively. These results confirmed the benefit of adding Fe species to MOF-5 for fabricating a novel bimetallic MOF with a higher surface area than the authentic MOFs. Besides, the remarkable role of Fe25/MOF-5 bimetallic MOF in boosting the inferior S_{BET} of CTS and directly enhancing its adsorption capacity. Notably, the mean pore size (Fig. 4B) of CTS, MOF-53(Fe), MOF-5, Fe25/MOF-5, and Fe25/MOF-5@CTS were 1.89, 2.01, 2.26, 2.98, 2.40 nm, respectively. This finding clarified

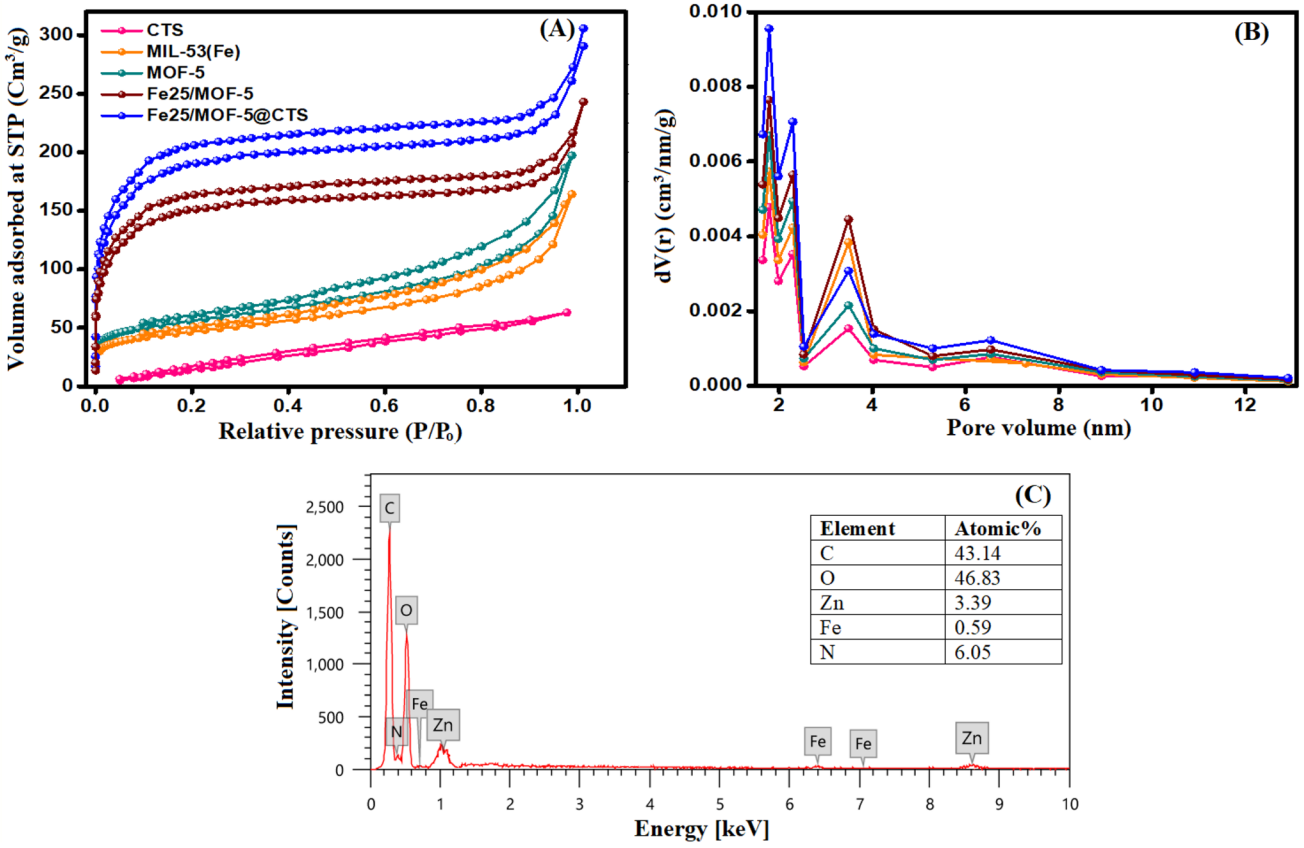

Fig. 4 BET measurements of CTS, MOF-53(Fe), MOF-5, Fe25/MOF-5, and Fe25/MOF-5@CTS; **A** Nitrogen adsorption/desorption isotherms, **B** Pore size distribution, and **C** SEM-EDX of Fe25/MOF-5@CTS

that Fe25/MOF-5 not only increases the CTS surface area but also improves its porosity.

SEM-EDX

SEM-EDX was utilized for defining the elemental composition of Fe25/MOF-5@CTS as elucidated in Fig. 4C. It was found that Fe25/MOF-5@CTS composed of C, O, Zn, Fe, and N with atomic percent 43.14, 46.83, 3.39, 0.59, and 6.05%. This finding inferred the successful combination between Fe25/MOF-5 and CTS.

XPS

The XPS wide-spectrum (Fig. 5A) implies the composition of Fe25/MOF-5@CTS composite film; C, O, N, Zn, and Fe with characteristic peaks manifested at 285.36, 532.74, 400.03, 1022.82, and 708.19 eV. The high-resolution C1s spectrum elucidated the related peaks to C–O/C–N, C–C/C–H, and O = C–O at 285.03, 284.49, and 288.37 eV (Fig. 5B). The high-resolution O1s spectrum (Fig. 5C) revealed two peaks at 533.60, and 531.77 eV which are accredited to M–O (viz., Zn–O, and Fe–O), and O = C–O. The high-resolution N1s spectrum (Fig. 5D) showed the belonging peaks to N–H at 399.54 eV. The high-resolution Fe spectrum (Fig. 5E) inferred the existence of Fe^{2+} at 711.19, and 725.54 eV as well as Fe^{3+} at 713.6 and 731.08 eV. The high-resolution Zn spectrum (Fig. 5F) pointed out the two characteristic XPS peaks to Zn2p1/2, and Zn2p3/2 at 1045.08, and 1022.03 eV.

Water Uptake and Mechanical Properties

Actually, the water uptake process primarily depends on the existence of free hydrophilic functional groups in the matrix. Fig.S1 shows the water uptake profiles of the pristine CTS and Fe25/MOF-5@CTS films. The results implied higher water uptake values of the CTS film compared to Fe25/MOF-5@CTS composite film. The water uptake value of the CTS film gradually increased from 63.56 to 131.07% when the test time increased from 0.5 to 3 h, owing to the hydrophilic nature of CTS. Thus, more water molecules can bind with the free hydrophilic OH and NH_2 groups of the CTS film. On the contrary, the incorporation of Fe25/MOF-5 adversely affected the affinity of chitosan towards the absorption of water molecules since the water uptake value was slightly elevated from 50.48 to 58.57% with increasing time from 0.5 to 3 h. These results may be due to the consumption of some hydrophilic groups via interaction with bi-metallic Fe/25MOF-5 during the composite formation. In addition, the mechanical properties of CTS and Fe25/MOF-5@CTS films were scrutinized, as represented in Table S1. Obviously, it was noticed an increase in the rigidity of the CTS film after the impregnation of Fe25/MOF-5. Therefore, the mechanical properties of Fe25/MOF-5@

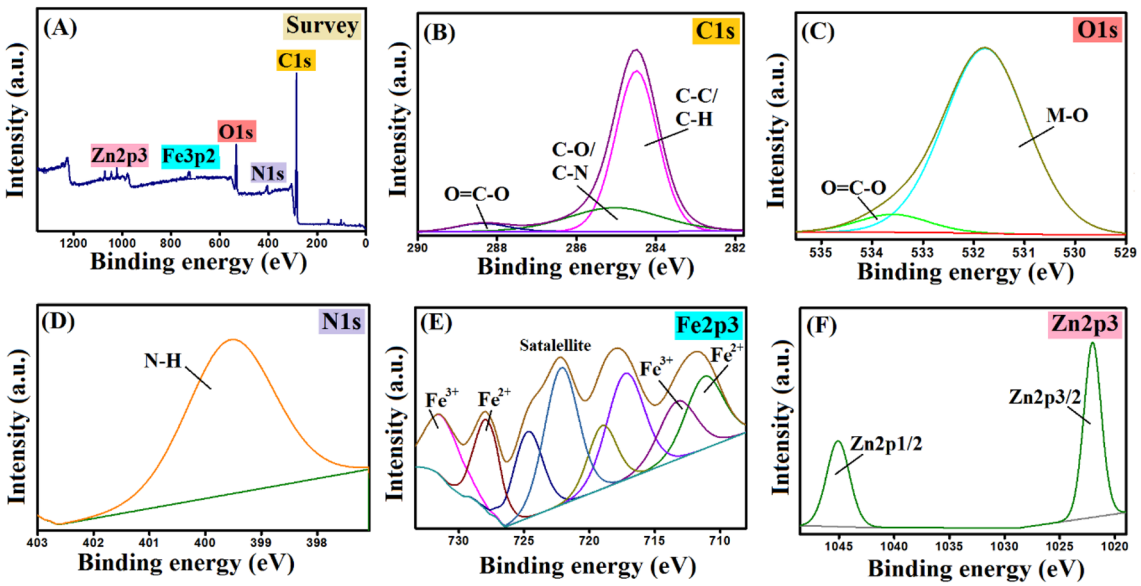

Fig. 5 XPS spectra of Fe25/MOF-5@CTS composite film; **A** Survey, **B** C1s, **C** O1s, **D** N1s, **E** Fe2p3, and **F** Zn2p3

CTS composite film were improved with a maximum force of 33.90 N and maximum strain of 6.70% needed to break Fe25/MOF-5@CTS composite film compared to 29.53 N and 2.70% for neat CTS film. Improvement of the mechanical properties could be associated with the strong interactions between Fe25/MOF-5 and CTS matrix.

Optimization of the CR Adsorption

Comparison Test

The comparison test (Fig. 6) consisted of two pivotal steps; the first step comprised determining the optimal ratio of Fe^{3+} in Fe/MOF-5 bimetallic MOF. Then, the introduced proportion of Fe^{3+} was tested in the range of 0–100 wt%. The experimental results showed that the adsorption capacity of CR by MOF-5, Fe25/MOF-5, Fe50/MOF-5, Fe75/MOF-5, and MIL-53(Fe) were 22.14, 78.50, 59.94, 51.06, and 47.64 mg/g, subsequently. Fe25/MOF-5 exhibited higher removal performance toward CR than the pristine MOF-5 and MIL-53(Fe) and the other fabricated bimetallic MOFs did.

Next, in the second step, Fe25/MOF-5 was doped onto the CTS film at a ratio of 0–10 wt%. It was recorded that the adsorption capacity of CR onto pure CTS was 41.81 mg/g, respectively. In addition, increasing the doped proportion of Fe25/MOF-5 from 1 to 5 wt% enhanced Q of CR from 49.79 to 77.06 mg/g, subsequently. Whereas the excessive increase in the doped percent of Fe25/MOF-5 in the film declined the adsorption capacity of CR to 58.39 mg/g, respectively. This decline in the adsorption performance is most probably due to the aggregation of Fe25/MOF-5 in the CTS matrix, blocking its pores and decreasing the surface area.

Consequently, the comparison test reflected the viability of doping the Fe25/MOF-5 bimetallic MOF into the CTS film to increase the adsorption capacity of the CTS film. Besides, decreasing the bimetallic MOF's cost by using a quite small amount of it and acquiring almost the same result as the pure bimetallic MOF.

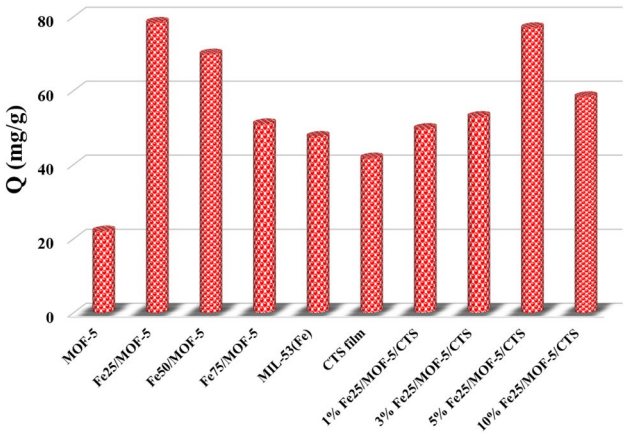

Fig. 6 Comparison test between the fabricated adsorbents

The Influence of pH

As a rule, pH controls the pollutant's ionization form, as well as the net surface charge of the adsorbent. Thence, the aptitude of the CR adsorption onto Fe25/MOF-5@CTS composite film was examined at a broad scale of pH as elucidated in Fig. 7A. It was observed a sharp decline in the adsorption capacity and R% from 77.06 mg/g and 77.74% to 41.22 mg/g and 42.96% when pH of CR solution elevated from 3 to 11, subsequently. Meanwhile, ZP results demonstrated the super high positive charge on the composite film's surface (56.3 mV) at pH 3, which decreased to 2.2 mV at pH 11 as a result of deprotonation of the composite functional groups. Based on the former results, the electrostatic forces are the predominant mechanism of CR adsorption onto the Fe25/MOF-5@CTS composite film [40]. Thus, the batch adsorption experiments were performed at pH 3. Interestingly, our work is limited to pH values above a certain threshold due to the potential dissolution of the CTS film at pH values below 3.

The Influence of the Dosage of Composite Film

Figure 7B illustrates the influence of the used amount of Fe25/MOF-5@CTS on the efficacy of CR removal. The raising in the weight of the used composite film in removing CR from 0.01 to 0.02 g boosted the CR removal% from 66.06 to 93.98%, subsequently. Such an enhancement in the CR removal aptitude can be explained by increasing the accessible active sites by elevating the composite film proportion [41]. Conversely, the increment in the proportion of Fe25/MOF-5@CTS dwindled the capacity of the adsorbed CR compared to available binding sites and incremented the empty binding sites [42].

The Influence of System Temperature

The thermodynamic performance of the system was deduced at a temperature range of 25–55 °C (Fig. 7C). It was monitored that this elevating in the system temperature sharply declined the R% and Q of CR onto Fe25/MOF-5@CTS from 77.74%, and 77.06 mg/g to 39.95%, and 38.12 mg/g, respectively, reflecting the exothermic behavior of the system. This drop in the CR removal aptitude is most likely due to the acceleration in the kinetic energy of the adsorbed CR, tending to the increase in the

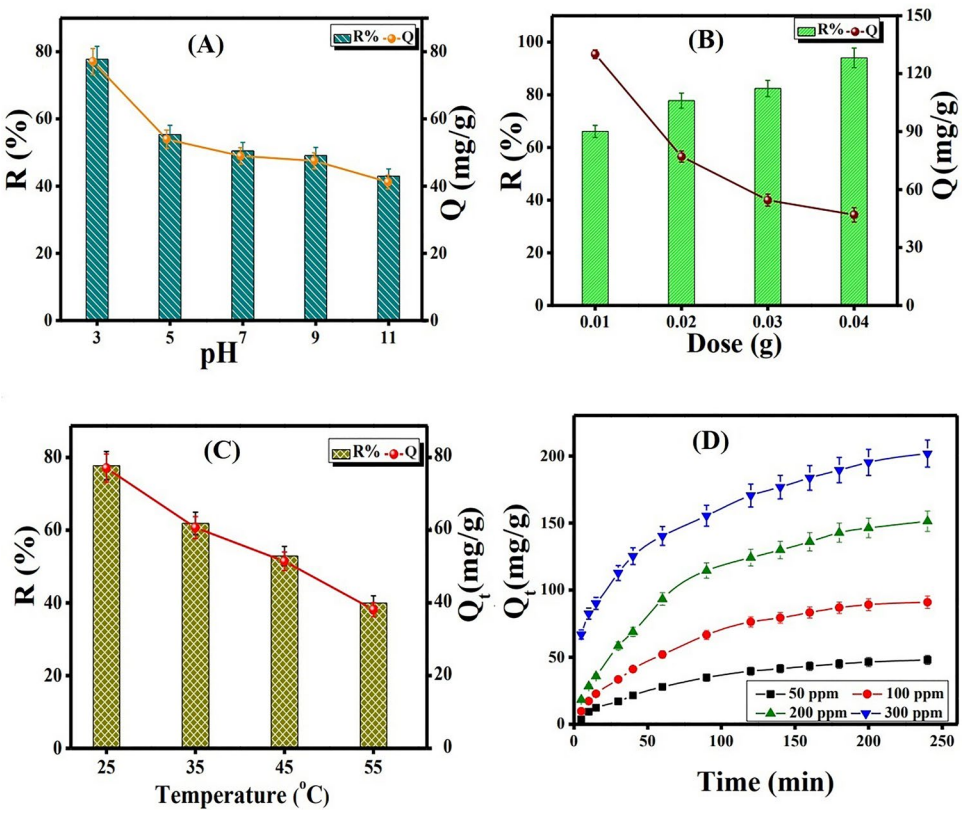

Fig. 7 Effect of **A** pH, **B** Dose, **C** Temperature, and **D** Initial concentration on the capacity of the CR adsorption onto Fe25/MOF-5@CTS composite film

CR desorption probability. Furthermore, the elevation in the temperature increments the CR Brownian motion, decreasing the adsorption probability of CR onto Fe25/MOF-5@CTS [43].

The Influence of the CR Concentration

Indeed, it is an essential point during setting up any adsorption system to identify the experimental maximum capacity (Q_{max}) of the adsorbent toward the targeted pollutants. Thence, the CR adsorption onto Fe25/MOF-5@CTS composite film was scrutinized at various concentrations of CR. Figure 7D implied an elevation in the Q_t of CR onto the composite film when the CR concentration uplifted from 50 to 300 ppm, revealing that the experimental Q_{max} was 201.81 mg/L. The acquired result could be explained by increasing the contaminant's driving forces toward the adsorbent surface by elevating the contaminant concentrations [44].

The Adsorption Mechanism of CR

Kinetics Study

For estimating the adsorption mechanism of CR onto Fe25/MOF-5@CTS composite film, the experimental results were analyzed kinetically by which Pseudo-1st -Order (PFO), Pseudo-2nd -Order (PSO), and Elovich (Fig. S2A-D). Table S2 represents the kinetic equations of the applied models. It was inferred the proceeding of the CR adsorption onto Fe25/MOF-5@CTS through the chemisorption pathway since the reckoned R^2 by PSO were greater than those of PFO (Table 1). Furthermore, the resemblance between $Q_{e,Exp}$, and the derived $Q_{e,Cal}$ from PSO is the second evidence of the chemisorption of CR [45]. Moreover, Elovich indicated the adsorption favorability of CR onto Fe25/MOF-5@CTS composite film in which the CR adsorption rate ($\alpha = 2.39–33.77$ mg/g.min) was much faster than the desorption rate ($\beta = 0.087–0.027$ g/mg).

Isotherms Study

Also, the obtained data from the experimental work were modeled isothermally by DR, Freundlich, Langmuir, and Temkin (Fig. S3A-D) to deduce the adsorption pathway of CR onto Fe25/MOF-5@CTS composite film. Table S3 summarizes the isotherm equations of these models. Isotherms analysis concluded the probability to adsorb CR onto Fe25/MOF-5@CTS via both chemisorption and physisorption pathways in which the R^2 values of Langmuir (0.977) and Freundlich (0.965) are almost similar (Table 2). Langmuir deduced that the Q_{max} of CR onto the composite film was 219.78 mg/g. In addition, Freundlich confirmed the CR

Table 1 Adsorption kinetic model parameters of the adsorption of CR onto Fe25/MOF-5@CTS composite film

Kinetic models and parameters	Concentration (ppm)				
	50	100	200	300	
$Q_{e,\ Exp}$ (mg/g)	45.05	86.89	142.78	189.46	
PFO					
$Q_{e,Cal}$ (mg/g)	48.03	93.01	124.68	135.69	
k_1 (min^{-1})	0.018	0.019	0.017	0.017	
R^2	0.983	0.977	0.992	0.976	
PSO					
$Q_{e,cal}$ (mg/g)	62.50	116.67	188.68	214.13	
k_2 ($g.mg^{-1}.min^{-1}$)	0.0002	0.0001	0.00008	0.0001	
R^2	0.993	0.994	0.995	0.991	
Elovich					
α (mg/g.min)	2.39	4.61	8.16	33.77	
β (g/mg)	0.081	0.043	0.026	0.027	
R^2	0.975	0.969	0.974	0.983	

Table 2 The parameters derived from isotherm models for the adsorption of the adsorption of CR onto Fe25/MOF-5@CTS composite film

Isotherm model	Parameter	Value
Langmuir	Q_{max} (mg/g)	219.78
	b (L/mg)	0.046
	R^2	0.977
Freundlich	n	2.26
	k_F (L/mg)	24.30
	R^2	0.965
Temkin	A (L/g)	0.532
	B (J/mol)	44.64
	b (KJ/mol)	0.056
	R^2	0.980
DR	Qs (mg/g)	144.88
	K_{DR} (mol^2/K^2J^2)	5.83×10^{-6}
	E (KJ/mol)	0.292
	R^2	0.777

adsorption preference onto the as-fabricated composite film in which n was over 2. Temkin suggested the physisorption mechanism of CR since b was 0.056 KJ/mol [46]. This finding was consistent with DR, which also indicated the proceeding of the adsorption of CR onto Fe25/MOF-5@CTS by physisorption in which E was 0.292 KJ/mol [47].

Hence, the acquired findings from kinetics and isotherms investigations denoted the possibility of the CR adsorption onto Fe25/MOF-5@CTS via physisorption and chemisorption pathways. So, Fe25/MOF-5@CTS composite film was analyzed by XPS after the CR adsorption to interpret the CR adsorption mechanisms. The XPS wide-spectrum (Fig. 8A) confirmed the CR adsorption onto Fe25/MOF-5@CTS in which the related peaks to S manifested at 168.22 eV with an increase in the N1s peak intensity. The high-resolution S2p3 spectrum (Fig. 8B) showed the two corresponding peaks to SO_3 groups of CR, S = O, and S–O at 167.85 and 169.92 eV. Besides, the high-resolution O1s spectrum (Fig. 8C) illustrated the concomitant peak of S = O at 532.38 eV. The mentioned findings confirmed the occurrence of the adsorption of CR onto the Fe25/MOF-5@CTS. The peaks shifting of M–O and O = C–O from 531.77 and 533.60 to 531.32 and 533.03 eV, suggest the contribution of the metal ions and the oxygen-containing functional groups of Fe25/MOF-5@CTS in the CR adsorption. Moreover, high-resolution Fe2p3 (Fig. 8D) and Zn2p3 (Fig. 8E) spectra elucidated peaks shifting to lower binding energy, which may be due to the formation of coordination bonds between Fe and Zn of Fe25/MOF-5@CTS and SO_3 and NH_2 of CR. Notably, it was previously deduced via the electron density map that the HOMO orbital's position in SO_3 of CR could interact with NH_2-containing adsorbent by host-guest interaction

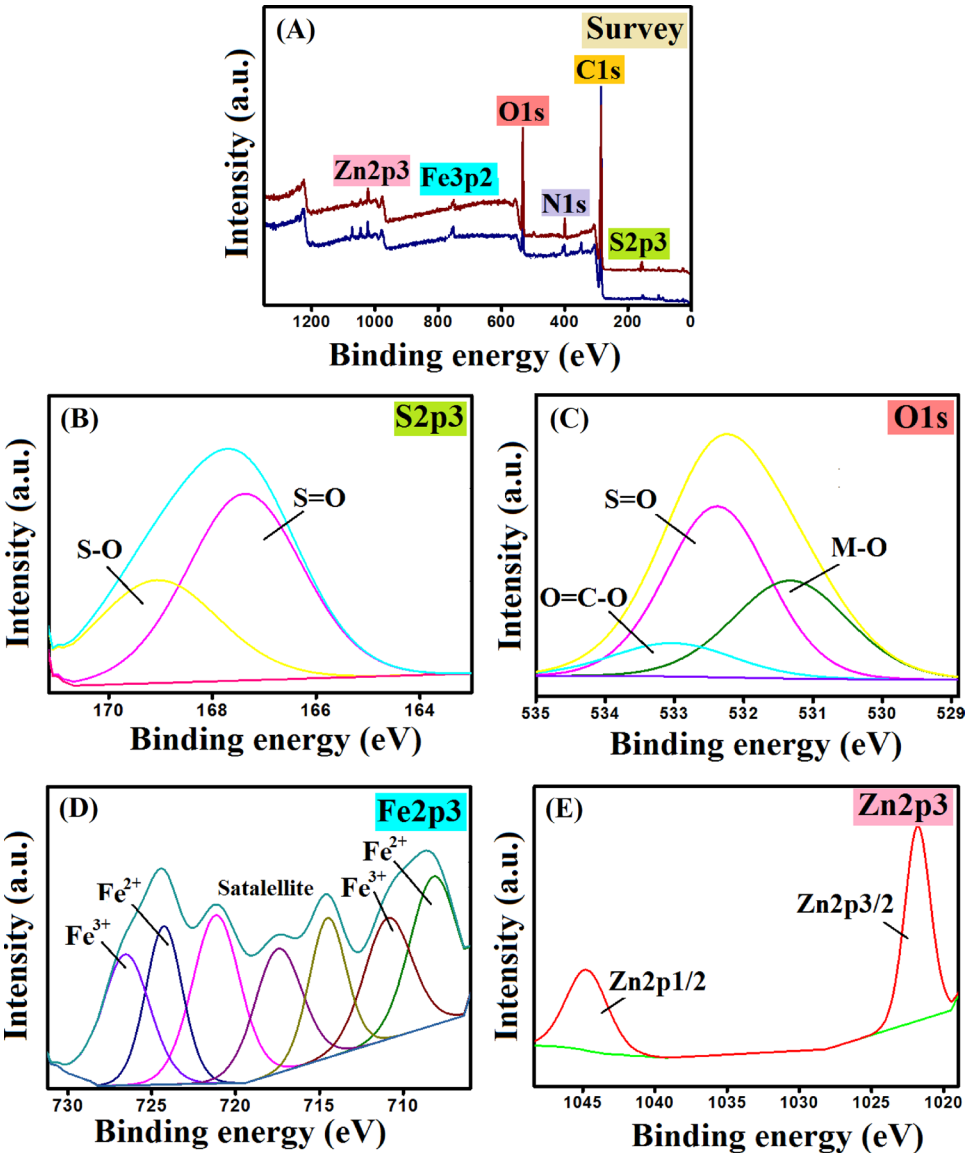

Fig. 8 XPS of Fe25/MOF-5@CTS composite film after the CR adsorption; **A** Survey, **B** S2p3, **C** O1s, **D** Fe2p3, and **E** Zn2p3

and electrostatic forces [48]. ZP and the impact of the pH medium results implied the vast prominence of the electrostatic force between the anionic CR and the highly positively charged Fe25/MOF-5@CTS composite film (ZP = 56.3 mV at pH 3). Moreover, host-gest interaction between CR and Fe25/MOF-5@CTS could occur via the H-bonding between the provided oxygenated groups on the composite film's surface (viz., COOH, OH) and H atoms of CR. Also, the SO_3 groups of CR could form an H-bonding with the H-atoms of Fe25/MOF-5@CTS. Noteworthy, the aromatic ring in both composite film and CR undoubtedly has an effective role in the CR adsorption onto Fe25/MOF-5@CTS via π-π interaction.

Shortly, kinetics and isotherms studies confirmed the CR adsorption by both chemisorption and physisorption pathways. In addition, XPS and ZP analyses and the experimental work indicated the proceeding of CR adsorption by physisorption pathway via electrostatic forces. Meanwhile, the chemisorption pathway of the CR adsorption could proceed via host-guest interaction, π-π interaction, and coordination bonds, as illustrated in Fig. 9. Interestingly, these clues suggested the suitability of our perspective that the small amount of the doped bimetallic MOF with varied functional groups could form strong interactions with CR and vastly boost the adsorbability of the CTS film.

The Impact of Ionic Strength

Figure 10 A exhibits the negative impact of the ionic strength on the capacity of the CR removal by Fe25/MOF-5@CTS composite film. It was observed a drop in the efficacy of the removal of CR since Q and R% declined to 50.95 mg/L and

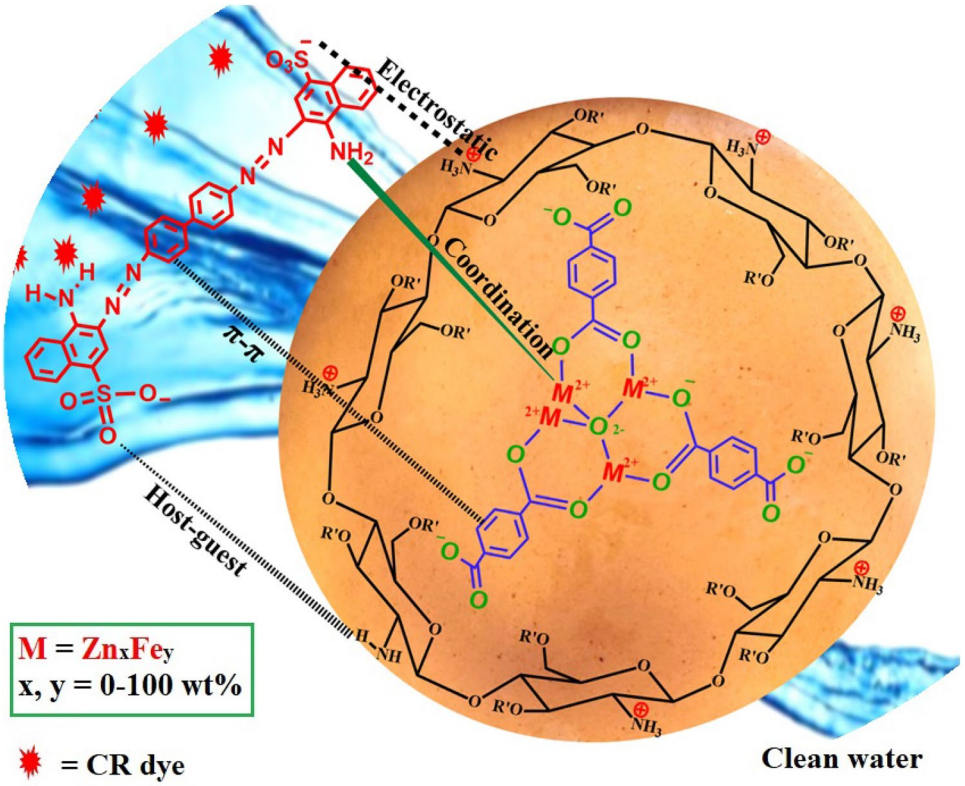

Fig. 9 The plausible mechanism of the CR adsorption onto Fe25/MOF-5@CTS composite film

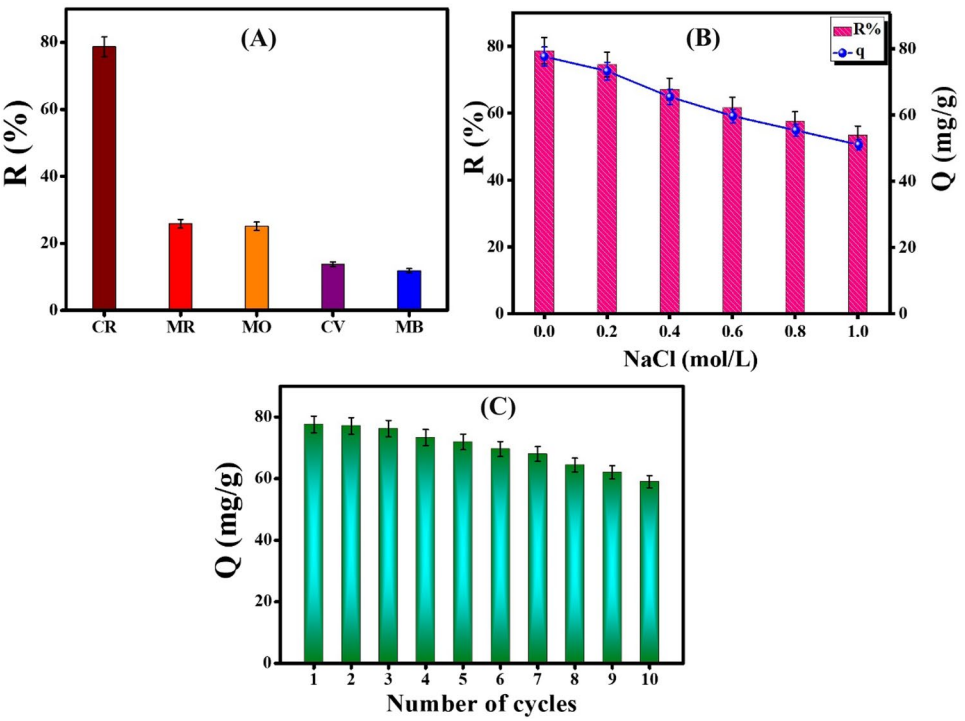

Fig. 10 **A** Effect of ionic strength on the CR adsorption, **B** Selectivity test, and **C** Cycling test of Fe25/MOF-5@CTS composite film

54.47% by raising the NaCl concentrations to 1.0 mol/L. Such a drop in the CR removal aptitude by Fe25/MOF-5@CTS may be attributed to the competition between Cl^- ions and CR for the positive active groups onto the composite film's surface, which was well consistent with Khan et al. [49].

Selectivity Test

For testing the adsorption selectivity of Fe25/MOF-5@CTS composite film toward CR, the removal capacity of other five common synthetic dyes by the as-fabricated composite film were scrutinized at the same adsorption conditions (Fig. 10B). Surprisingly, Fe25/MOF-5@CTS exhibited a superior removal capacity of CR compared to the other cationic and anionic dyes in which R% of CR, MR, MO, MB, and CV were 78.74, 25.91, 25.13, 11.87, and 13.75%, subsequently. The concrete results reflected the more eminent selectivity of Fe25/MOF-5@CTS towards the anionic dyes, especially CR than the cationic dyes. This selectivity behavior is most likely due to the plenty of positive active groups on the surface of the composite film that enable it to attract the anionic dyes via the electrostatic forces. The higher removal aptitude of Fe25/MOF-5@CTS towards CR that attained 3-folds of the other anionic dyes is most probably owing to the plenty of NH_2 onto the CR surface that could be attached to the metals of the composite film via the coordination bonds. While both MO and MR contain only $N(CH3)_2$ group which has a lower affinity to form coordination bonds with Fe25/MOF-5@CTS. In addition to the abundant SO_3^- in the CR structure that could interact with Fe25/MOF-5@CTS via electrostatic and host-guest interactions. Whereas MO contains less number of SO_3^- group than CR, thus the interactions between MO and Fe25/MOF-5@CTS are weaker than those of CR. Notably, the difficulty of deprotonation of the COOH group of MR in the acidic medium prevents the occurrence of electrostatic interactions between MO and Fe25/MOF-5@CTS.

Cycling Test

To prove the viability of our strategy to fabricate efficient and recyclable adsorbent with reduced cost, it was an intrinsic issue to assess the renewability of Fe25/MOF-5@CTS composite film. The cycling test (Fig. 10C) revealed the supreme reusability of the as-fabricated composite film for removing CR with a trivial loss in its adsorption capacity was about 18.54 mg/g after ten successive cycles. The inconsiderable decrease in the adsorption capacity of Fe25/MOF-5@CTS may be due to the strong chemical interactions between the composite film and CR that prevent the complete elution of CR. Finally, such auspicious results suggested the excellent efficacy, stability, selectivity, and recyclability of Fe25/MOF-5@CTS composite film and its viability to expand out of lab scale to industrial scale.

Durability Study

To prove the durability of Fe25/MOF-5@CTS, the crystallinity and S_{BET} of the used composite film were characterized using XRD and BET. In addition, the metal leaching was examined by analyzing the authentic and used composite films utilizing SEM-EDX. Figure 11A illustrates the XRD of pristine and used Fe25/MOF-5@CTS composite films. It was noticed the appearance of the same diffraction peaks of Fe25/MOF-5@CTS after the CR adsorption with a slight diminution in the peak intensity. These observations confirmed the stability of the chemical structure of Fe25/MOF-5@CTS, while the slight decline in the Fe25/MOF-5@CTS crystallinity confirmed proceeding the adsorption process of CR onto the composite film's surface. The BET measurements (Fig. 11B) clarified a slight decrease in the S_{BET} of Fe25/MOF-5@CTS from 516.54 to 414.22 m^2/g after the CR adsorption owes to occupying the surface and the pores of the composite film by the CR molecules. SEM-EDX of the used Fe25/MOF-5@CTS composite film (Fig. 11C) revealed inconsiderable diminution in the atomic% of Zn and Fe species by about 0.09 and 0.04%, respectively. In addition, the increase in the atomic% of nitrogen and the manifestation of the distinctive peaks of sulfur, indicate the CR adsorption onto Fe25/MOF-5@CTS. The stable chemical structure, slight decrease in S_{BET}, and low metal leaching after the CR adsorption proved the durability of Fe25/MOF-5@CTS composite film.

Conclusion

The study utilized a cost-effective approach to foster the adsorption capacity of the CTS film by decorating it with a small proportion of Fe25/MOF-5 bimetallic MOF, forming an efficient and durable composite film. The ZP results showed the frequently high positive charges onto the Fe25/MOF-5@CTS composite film attained 56.3 mV. The water uptake test exhibited the lower water uptake performance of the Fe25/MOF-5@CTS composite film than the neat CTS. In addition to the advanced mechanical property of the Fe25/MOF-5@CTS composite film, compared to the CTS film. The practical experimental showed that the optimal conditions to adsorb CR onto Fe25/MOF-5@CTS were at pH = 3 and using a composite film dosage of about 0.01 g at room temperature. The selectivity test confirmed the high affinity of the as-fabricated composite film toward the CR molecules. Furthermore, the cycling test affirmed the viability of the used strategy to obtain a

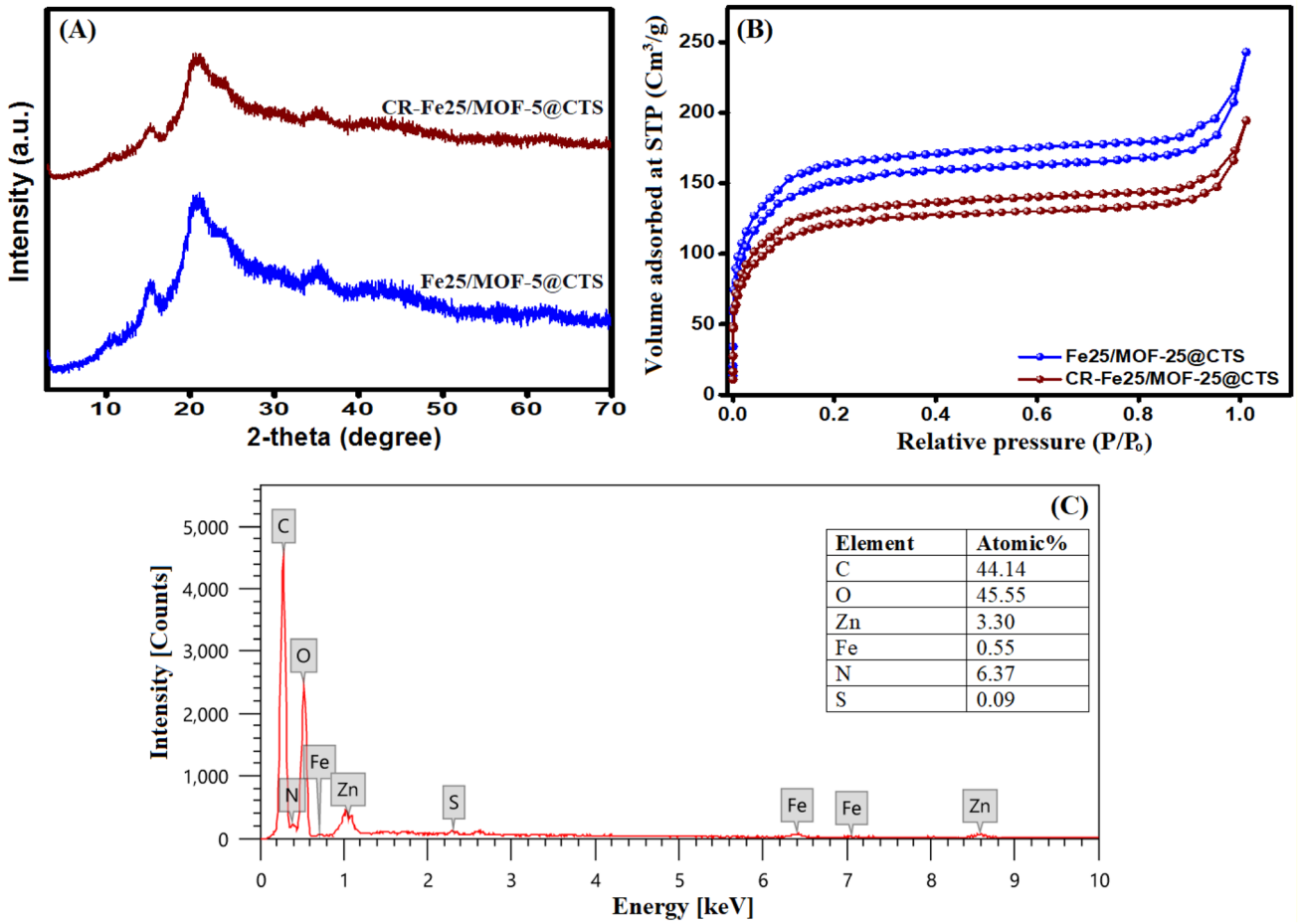

Fig. 11 **A** XRD, **B** BET measurements of fresh and used Fe25/MOF-5@CTS, and **C** SEM-EDX of used Fe25/MOF-5@CTS

durable composite film with recyclability merit, where the loss in the adsorption aptitude of Fe25/MOF-5@CTS composite film after the 10th cycle was 18.54 mg/g. Isotherms study indicated the appropriateness of both Langmuir and Freundlich to represent the CR adsorption onto Fe25/MOF-5@CTS. Whereas, the kinetics study denoted the aptness of PSO to symbolize the adsorption of CR. Host-guest interaction, π-π interaction, electrostatic interaction and coordination bonds were found to be the possible interactions between CR molecules and Fe25/MOF-5@CTS. Ultimately, the characterization tools and the practical experiments proved the viability of this technique to boost the adsorption capacity of CTS by doping its matrix with a small amount with the efficient Fe25/MOF-5@CTS. Interestingly, this strategy renders the adsorption capacity of the cost-effectiveness CTS almost similar to the quite expensive materials like MOFs.

Supplementary Information The online version contains supplementary material available at https://doi.org/10.1007/s10924-023-03123-2.

Author Contributions AE, EA: Conceptualization, Methodology, Validation, Data curation, Writing—original draft, Writing—review and editing, Resources, Formal analysis, Visualization; AO: Conceptualization, Resources, Writing—review and editing.

Funding Open access funding provided by The Science, Technology & Innovation Funding Authority (STDF) in cooperation with The Egyptian Knowledge Bank (EKB). No funding was received to assist with the preparation of this manuscript.

Data Availability All data are included in the manuscript and supplementary information.

Declarations

Conflict of interest The authors declare that they have no known competing financial interests or personal relationships that could have appeared to influence the work reported in this paper.

References

1. Liu J, Wang N, Zhang H, Baeyens J (2019) Adsorption of Congo red dye on FexCo3-xO4 nanoparticles. J Environ Manage 238:473–483
2. Eltaweil AS, Bakr SS, Abd El-Monaem EM, El-Subruiti GM (2023a) Magnetic hierarchical flower-like Fe_3O_4@ ZIF-67/CuN-iMn-LDH catalyst with enhanced redox cycle for fenton-like degradation of congo red: optimization and mechanism. Environ Sci Pollut Res. 30:1–17
3. Koohi P, Rahbar-kelishami A, Shayesteh H (2021) Efficient removal of Congo red dye using Fe3O4/NiO nanocomposite: synthesis and characterization. Environ Technol Innov 23:101559
4. Ghorai S, Sarkar AK, Panda AB, Pal S (2013) Effective removal of Congo red dye from aqueous solution using modified xanthan gum/silica hybrid nanocomposite as adsorbent. Bioresour Technol 144:485–491
5. Kristianto H, Rahman H, Prasetyo S, Sugih AK (2019) Removal of Congo red aqueous solution using Leucaena leucocephala seed's extract as natural coagulant. Appl Water Sci 9(4):1–7
6. Kristianto H, Tanuarto M, Prasetyo S, Sugih A (2020) Magnetically assisted coagulation using iron oxide nanoparticles-Leucaena leucocephala seeds' extract to treat synthetic Congo red wastewater. Int J Environ Sci Technol 17(7):3561–3570
7. Cai T, Chen H, Yao L, Peng H (2023) 3D hierarchical porous and N-Doped carbonized microspheres derived from chitin for remarkable adsorption of congo red in aqueous solution. Int J Mol Sci 24(1):684
8. Gerulová K, Sanny Z, Kucmanová A, Buranská E (2021) Preliminary Study into the decolorization of selected dyes by the ozone application. Vedecké Práce Materiálovotechnologickej Fakulty Slovenskej Technickej Univerzity v Bratislave so. Sídlom v Trnave 29(48):37–44
9. Gupta A, Khan SA, Khan TA (2021) Remediation of Textile Wastewater by Ozonation. Sustainable Practices in the Textile Industry Wiley, Hoboken, pp 273–284
10. Abd El-Monaem EM, Elshishini HM, Bakr SS et al (2023b) A comprehensive review on LDH-based catalysts to activate persulfates for the degradation of organic pollutants. npj Clean Water 6(1):34
11. Radoor S, Karayil J, Parameswaranpillai J, Siengchin S (2020) Removal of anionic dye Congo red from aqueous environment using polyvinyl alcohol/sodium alginate/ZSM-5 zeolite membrane. Sci Rep 10(1):1–15
12. Tan Y, Kang Y, Wang W et al (2021) Chitosan modified inorganic nanowires membranes for ultra-fast and efficient removal of Congo red. Appl Surf Sci 569:150970
13. Ahmad R, Ansari K (2021) Comparative study for adsorption of Congo red and methylene blue dye on Chitosan modified hybrid nanocomposite. Process Biochem 108:90–102
14. Evans JD, Sumby CJ, Doonan CJ (2014) Post-synthetic metalation of metal–organic frameworks. Chem Soc Rev 43(16):5933–5951
15. Hwang YK, Hong DY, Chang JS et al (2008) Amine grafting on coordinatively unsaturated metal centers of MOFs: consequences for catalysis and metal encapsulation. Angew Chem 120(22):4212–4216
16. Khan MS, Khalid M, Shahid M (2020) What triggers dye adsorption by metal organic frameworks? The current perspectives. Mater Adv 1(6):1575–1601
17. Chaemchuen S, Kabir NA, Zhou K, Verpoort F (2013) Metal–organic frameworks for upgrading biogas via CO_2 adsorption to biogas green energy. Chem Soc Rev 42(24):9304–9332
18. Abd El-Monaem EM, Omer AM, Khalifa RE, Eltaweil AS (2022) Floatable cellulose acetate beads embedded with flower-like zwitterionic binary MOF/PDA for efficient removal of tetracycline. J Colloid Interface Sci 620:333–345
19. Zhang X, Luo J, Wan K et al (2019) From rational design of a new bimetallic MOF family with tunable linkers to OER catalysts. J Mater Chem A 7(4):1616–1628
20. Abd El-Monaem EM, Eltaweil AS, El-Subruiti GM, Mohy-Eldin MS, Omer AM (2023c) Adsorption of nitrophenol onto a novel Fe3O4-κ-carrageenan/MIL-125 (Ti) composite: process optimization, isotherms, kinetics, and mechanism. Environ Sci Pollut Res 30(17):49301–49313. https://doi.org/10.1007/s11356-023-25678-2
21. Mosavi SH, Zare-Dorabei R, Bereyhi M (2021) Rapid and effective ultrasonic-assisted adsorptive removal of Congo Red onto MOF-5 modified by $CuCl_2$ in ambient conditions: adsorption isotherms and kinetics studies. ChemistrySelect 6(18):4432–4439
22. Mohammadi AA, Moghanlo S, Kazemi MS et al (2022) Comparative removal of hazardous cationic dyes by MOF-5 and modified graphene oxide. Sci Rep 12(1):1–12
23. Othman NW, Radde H, Puah PY, Ling YS, Moh PY (2019) Enhancing photocatalytic activity of titanium dioxide through incorporation of MIL-53 (fe) toward degradation of organic dye. J Chin Chem Soc 66(1):81–88
24. Omer AM, Elgarhy GS, El-Subruiti GM, Abd El-Monaem EM, Eltaweil AS (2023) Construction of efficient Ni-FeLDH@MWCNT@ cellulose acetate floatable microbeads for cr (VI) removal: performance and mechanism. Carbohydr Polym 311:120771
25. Kou SG, Peters LM, Mucalo MR (2021) Chitosan: a review of sources and preparation methods. Int J Biol Macromol 169:85–94
26. Ali MEA, Aboelfadl MMS, Selim AM, Khalil HF, Elkady GM (2018) Chitosan nanoparticles extracted from shrimp shells, application for removal of Fe (II) and mn (II) from aqueous phases. Sep Sci Technol 53(18):2870–2881
27. Badawy ME, Lotfy TM, Shawir S (2019) Preparation and antibacterial activity of chitosan-silver nanoparticles for application in preservation of minced meat. Bull Natl Res Centre 43(1):1–14
28. Greer HF, Liu Y, Greenaway A, Wright PA, Zhou W (2016) Synthesis and formation mechanism of textured MOF-5. Cryst Growth Des 16(4):2104–2111
29. Tirmizi SA, Badshah A, Ammad HM et al (2018) Synthesis of highly stable MOF-5@ MWCNTs nanocomposite with improved hydrophobic properties. Arab J Chem 11(1):26–33
30. Chaturvedi G, Kaur A, Kansal SK (2019) CdS-decorated MIL-53 (fe) microrods with enhanced visible light photocatalytic performance for the degradation of ketorolac tromethamine and mechanism insight. J Phys Chem C 123(27):16857–16867
31. El-Yazeed WA, Abou El-Reash Y, Elatwy L, Ahmed AI (2020) Facile fabrication of bimetallic Fe–Mg MOF for the synthesis of xanthenes and removal of heavy metal ions. RSC Adv 10(16):9693–9703

32. Drabczyk A, Kudłacik-Kramarczyk S, Głąb M et al (2020) Physicochemical investigations of Chitosan-based hydrogels containing Aloe Vera designed for biomedical use. Materials 13(14):3073
33. Pasandideh Y, Razmi H (2022) Introduction of a Zn-based metal–organic framework@ biomass porous activated carbon as a high-sensitive coating for a stainless steel SPME fiber: application to the simultaneous analysis of nonsteroidal anti-inflammatory Drugs. BMC Chem 16(1):1–16
34. Nguyen DTC, Le HTN, Do TS et al (2019) Metal-organic framework MIL-53 (Fe) as an adsorbent for ibuprofen drug removal from aqueous solutions: response surface modeling and optimization. J Chem 2019:5602957
35. Omer AM, Abd El-Monaem EM, El-Subruiti GM, Abd El-Latif MM, Eltaweil AS (2021) Fabrication of easy separable and reusable MIL-125 (Ti)/MIL-53 (fe) binary MOF/CNT/Alginate composite microbeads for tetracycline removal from water bodies. Sci Rep 11(1):23818
36. Lima HA, Lia FMV, Ramdayal S (2014) Preparation and characterization of chitosan-insulin-tripolyphosphate membrane for controlled drug release: effect of cross linking agent. J Biomaterials Nanobiotechnol 5(04):211
37. Merz CR (2019) Physicochemical and colligative investigation of α (shrimp shell)-and β (squid pen)-chitosan membranes: concentration-gradient-driven water flux and ion transport for salinity gradient power and separation process operations. ACS Omega 4(25):21027–21040
38. Abolhassani M, Griggs CS, Gurtowski LA et al (2017) Scalable chitosan-graphene oxide membranes: the effect of GO size on properties and cross-flow filtration performance. ACS Omega 2(12):8751–8759
39. Gümüşderelioğlu M, Sunal E, Tolga Demirtaş T, Kiremitçi AS (2020) Chitosan-based double-faced barrier membrane coated with functional nanostructures and loaded with BMP-6. J Mater Science: Mater Med 31:1–14
40. Abd El-Monaem EM, Ayoup MS, Omer AM, Hammad EN, Eltaweil AS (2023a) Sandwich-like construction of a new aminated chitosan Schiff base for efficient removal of Congo red. Appl Water Sci 13(2):67
41. Sime T, Fito J, Nkambule TT, Temesgen Y, Sergawie A (2023) Adsorption of congo red from textile wastewater using activated carbon developed from corn cobs: the studies of isotherms and kinetics. Chem Afr. https://doi.org/10.1007/s42250-022-00583-2
42. Omer AM, Abd El-Monaem EM, Eltaweil AS (2022) Novel reusable amine-functionalized cellulose acetate beads impregnated aminated graphene oxide for adsorptive removal of hexavalent chromium ions. Int J Biol Macromol 208:925–934
43. Ayawei N, Godwin J, Wankasi D (2015) Synthesis and sorption studies of the degradation of Congo Red by Ni–Fe layered double hydroxide. Int J Appl Chem Sci Res 13(3):1197–1217
44. Kamil AM, Mohammed HT, Alkaim AF, Hussein FH (2016) Adsorption of Congo red on multiwall carbon nanotubes: Effect of operational parameters. J Chem Pharm Sci 9(3):1128–1133
45. Eltaweil AS, Ibrahim K, Abd El-Monaem EM, El-Subruiti GM, Omer AM (2023b) Phosphate removal by Lanthanum-doped aminated graphene oxide@ aminated chitosan microspheres: insights into the adsorption mechanism. J Clean Prod 385:135640
46. Erhayem M, Al-Tohami F, Mohamed R, Ahmida K (2015) Isotherm, kinetic and thermodynamic studies for the sorption of mercury (II) onto activated carbon from Rosmarinus officinalis leaves. Am J Anal Chem 6(01):1
47. Balarak D, Kord Mostafapour F, Azarpira H, Joghataei A (2017) Langmuir, Freundlich, Temkin and Dubinin-Radushkevich isotherms studies of equilibrium sorption of ampicilin unto montmorillonite nanoparticles. J Pharm Res Int 20:1–9
48. Valadi FM, Ekramipooya A, Gholami MR (2020) Selective separation of Congo Red from a mixture of anionic and cationic dyes using magnetic-MOF: experimental and DFT study. J Mol Liq 318:114051
49. Khan MI, Akhtar S, Zafar S et al (2015) Removal of Congo red from aqueous solution by anion exchange membrane (EBTAC): adsorption kinetics and themodynamics. Materials 8(7):4147–4161